Supporting information for

Rare-earth Co-doping Promotes High-capacity and Long-cycle Ni-rich Layered Oxide Cathodes via Lattice Stabilization and Interface Engineering

*Yan Xin, Chen Wang, Fang Zhang, Bijiao He, Zizheng Li, Huajun Tian**

Beijing Laboratory of New Energy Storage Technology and Key Laboratory of Power Station Energy Transfer Conversion and System of Ministry of Education, School of Energy Power and Mechanical Engineering, North China Electric Power University, Beijing 102206, China

*Corresponding authors: Huajun.Tian@ncepu.edu.cn (H.J. Tian)

Experimental

Materials Synthesis

The $LiNi_{0.9}Co_{0.05}Al_{0.05}Nd_{0.01}O_2$ (NCA), $LiNi_{0.9}Co_{0.04}Al_{0.05}Nd_{0.01}O_2$ (NCANd), $LiNi_{0.9}Co_{0.04}Al_{0.05}Ce_{0.01}O_2$ (NCACe), $LiNi_{0.9}Co_{0.04}Al_{0.05}Y_{0.01}O_2$ (NCAY), $LiNi_{0.9}Co_{0.04}Al_{0.05}Yb_{0.01}O_2$ (NCAYb) $LiNi_{0.9}Co_{0.038}Al_{0.05}Yb_{0.01}Y_{0.002}O_2$ (NCAYbY) cathodes were synthesized via a co-precipitation method in a 10 L continuous stirred-tank reactor (CSTR) and one-step calcination process.

Stoichiometric amounts of $NiSO_4 \cdot 6H_2O$ (99%, Aladdin), $CoSO_4 \cdot 7H_2O$ (99%, Aladdin), $Nd_2(SO_4)_3 \cdot 8H_2O$ (99.9%, Aladdin), $Ce(SO_4)_2 \cdot 4H_2O$ (98%, Aladdin), $Y_2(SO_4)_3 \cdot 8H_2O$ (99.9%, Aladdin), $Yb_2(SO_4)_3 \cdot 8H_2O$ (99.9%, Aladdin) and $Al_2(SO_4)_3 \cdot 18H_2O$ (99%, Aladdin) were dissolved in deionized (DI) water. The Ni/Co/Nd/Ce/Y/Yb mixed solution and Al solution were each prepared with a volume of 150 mL. EDTA-2Na·$2H_2O$ (98%, Aladdin) was added to the Al solution in an equimolar amount to Al^{3+}.

The reactor was initially filled with 5 L of $NH_3 \cdot H_2O$ (0.5-1.3 mol L^{-1}) as the base solution and heated to 60 °C. During precipitation, the pH was maintained at 10.2-11.8 by supplementing with 2 mol L^{-1} NaOH under continuous stirring at 600 rpm. The optimized parameters are 1 mol L^{-1} ammonia solution with a pH of 11. The metal salt solutions were then pumped into the reactor at a constant flow rate for 4 h under an Ar atmosphere. After addition, the resulting slurry was aged for 12 h without stirring, followed by filtration, thorough washing with DI water and drying in a vacuum oven at 100 °C for 12 h. The obtained precursors were thoroughly mixed LiOH with a 5 wt.% excess relative to the stoichiometric Li content, and then the mixtures were heated at 500 °C for 1 h and at 730 °C for 11 h under a flowing oxygen atmosphere to obtain cathode materials.

In order to eliminate the influence caused by the decrease in Co content, we also synthesized two undoped control NCA samples using the identical synthetic procedure: $LiNi_{0.9}Co_{0.04}Al_{0.05}O_2$ with the identical Co content as NCAYb/NCAY, and $LiNi_{0.9}Co_{0.038}Al_{0.05}O_2$ matching the Co content of the Yb/Y co-doped NCAYbY sample.

Material Characterizations

The phase composition and structural characteristics were analyzed by powder X-ray diffraction (XRD, SmartLab) with Cu Kα radiation (λ =1.5405 Å), in the 2θ range of 10–80° at a scan rate of 2° min-1. Rietveld refinement was performed using the Fullprof software. Guided by density functional theory (DFT) results that confirmed preferential occupation of transition-metal sites, Y/Yb were constrained at TM positions during Rietveld fitting. In FullProf Rietveld refinement of Li^+/Ni^{2+} disorder for cathodes, constraints were applied to maintain site occupancy conservation. A free variable x was defined to represent the fraction of Ni occupying the Li layer (3*a* sites) and the fraction of Li occupying the transition metal layer (3*b* sites). Then, the constraints for the Li occupancy at the 3*a* sites and the Ni occupancy at the 3*b* sites were $1\text{-}x$ and $0.9\text{-}x$, respectively. X-ray photoelectron spectroscopy (XPS, Thermo Nexsa G2) was carried out to probe surface compositions and element valence states. The spectra were fitted using Avantage software and the relative concentrations of different chemical states were established based on the split-peak fitting results.

The morphology and element distributions were examined by scanning electron microscopy (SEM, Hitachi SU1000) and energy-dispersive spectroscopy (EDS, Oxford EMAX), respectively. Particle size distributions were measured by a laser particle size analyzer (Fritsch Analysette 22 NeXT Nano). The chemical compositions of the cathodes were determined by Inductively coupled plasma mass spectrometry (ICP-MS, PerkinElmer NexION 2200G). High-resolution transmission electron microscopy (HRTEM, FEI Tecnai G2F20) was used to observe the microstructure and collect the lattice fringe images and fast Fourier transform (FFT) patterns. The surface roughness, morphological integrity and Young’s modulus distribution of the cycled electrode sheets were characterized by atomic force microscopy (AFM, Dimension Icon). Differential scanning calorimetry (DSC, PerkinElmer DSC 6000) was performed in an air atmosphere at a heating rate of 5 °C min^{-1} to assess thermal stability.

Electrochemical Measurement

The CR2032 coin-type cells were fabricated in an Ar-filled glove box (H_2O and O_2 < 0.01 ppm) for electrochemical assessment, using Celgard 2500 as the separator and

80 μL electrolyte per cell. The electrolyte consisted of a 1.2 M $LiPF_6$ solution in a mixture of ethylene carbonate (EC) and ethyl methyl carbonate (EMC) (volume ratio of 3:7) with 2.0% vinylene carbonate (VC) as an additive.

For cathode preparation, the active material, conductive carbon black (Super P), and polyvinylidene fluoride (PVDF) binder were mixed in a mass ratio of 8:1:1 in N-methyl-2-pyrrolidone (NMP) and stirred for 6 h to form a uniform slurry. Then, the slurry was coated onto aluminum foil and vacuum dried at 120 °C for 12 h. Finally, the dried sheet is punched into circular cathode plates with a diameter of 12 mm, with active material mass loading of 2.0 to 3.0 mg cm^{-2}.

Half cells were assembled utilizing the prepared the prepared cathode plates and Li metal as the counter/reference electrode. For full cells, anodes were prepared by mixing 80 wt.%, 10 wt.% Super P and 10 wt.% PVDF in NMP, casting the slurry onto copper foil, vacuum-drying at 80 °C for 12 hours, and punching into 14 mm discs. The negative-to-positive capacity ratio (N/P ratio) was controlled between 1.15:1 and 1.2:1 in the full cells.

Galvanostatic charge-discharge (GCD) tests were performed using a battery tester (Land, Wuhan). After three formation cycles at 0.2 C (1 C = 180 mAh g^{-1}) at room temperature, cycling stability was evaluated at 0.2, 1, 3, and 5 C. Rate capability was assessed at 0.1, 0.2, 0.5, 1.0, 2.0, 5.0 and 10 C, followed by a recovery step at 0.1 C.

The Li^+ diffusion kinetic behavior was investigated using the galvanostatic intermittent titration technique (GITT) at 0.2C, with each with current pulse lasting 5 min and a subsequent resting time of 30 min. Cyclic voltammetry (CV) and electrochemical impedance spectroscopy (EIS) were conducted using a high precision electrochemical workstation (PARSTAT MC). CV was recorded at scan rates of 0.1-0.5 mV s^{-1} in the voltage range of 2.7-4.3 V. EIS was performed using a dual-electrode cell with a potential amplitude of 5 mV over a frequency range of 100 kHz to 0.01 Hz. In situ distribution of relaxation times (DRT) analysis based on in situ EIS data acquired at the 5th, 100th, and 200th discharge cycles in the voltage range of 3.7-4.3 V to characterize electrochemical behavior at different states of charge (SOCs).

DFT Calculations

First-principles calculations were performed using density functional theory (DFT) as implemented in the Vienna Ab initio Simulation Package (VASP).[1,2] The electron-ion interactions were described using the projector augmented-wave (PAW) method.[3] The exchange-correlation functional was described using the Perdew-Burke-Ernzerhof (PBE) generalized gradient approximation (GGA).[4,5] To properly account for the strong electron correlations, the DFT+U approach in the Dudarev formalism was employed.[6] The effective on-site Coulomb interaction parameters (U) of 3.0, 4.0, 7.0, and 9.0 eV were assigned to the d orbitals of Co, Ni, and Y and the f orbitals of Yb, respectively.[7–9] The initial magnetic moments of Co, Ni, Y, and Yb were set to 5 μB. A plane-wave basis set with an energy cutoff of 600 eV was used.

For the $LiNiO_2$-based system, a 2×2×2 supercell containing 108 atoms was constructed to model pristine and doped structures. The Brillouin zone was sampled using a Monkhorst-Pack k-point mesh of 3×3×2 for structural relaxation of the following cathode systems: $Li_{27}(Ni_{25}Co_1Al_1)O_{54}$ (NCA), $Li_{27}(Ni_{23}Co_1Al_1Yb_1Y_1)O_{54}$ (Yb@TM/Y@TM, NCAYbY), $(Li_{26}Y_1)(Ni_{24}Co_1Al_1Yb_1)O_{54}$ (Yb@TM/Y@Li), $(Li_{26}Yb_1)(Ni_{24}Co_1Al_1Y_1)O_{54}$ (Yb@Li/Y@TM), and $(Li_{25}Yb_1Y_1)(Ni_{25}Co_1Al_1)O_{54}$ (Yb@Li/Y@Li). The corresponding structural diagrams are shown in Figure S16. The electronic self-consistent field cycle was considered converged when the total energy change between successive steps was less than 1×10^{-6} eV. Geometry optimization was performed until the Hellmann-Feynman forces on all atoms were below 0.02 eV $Å^{-1}$.

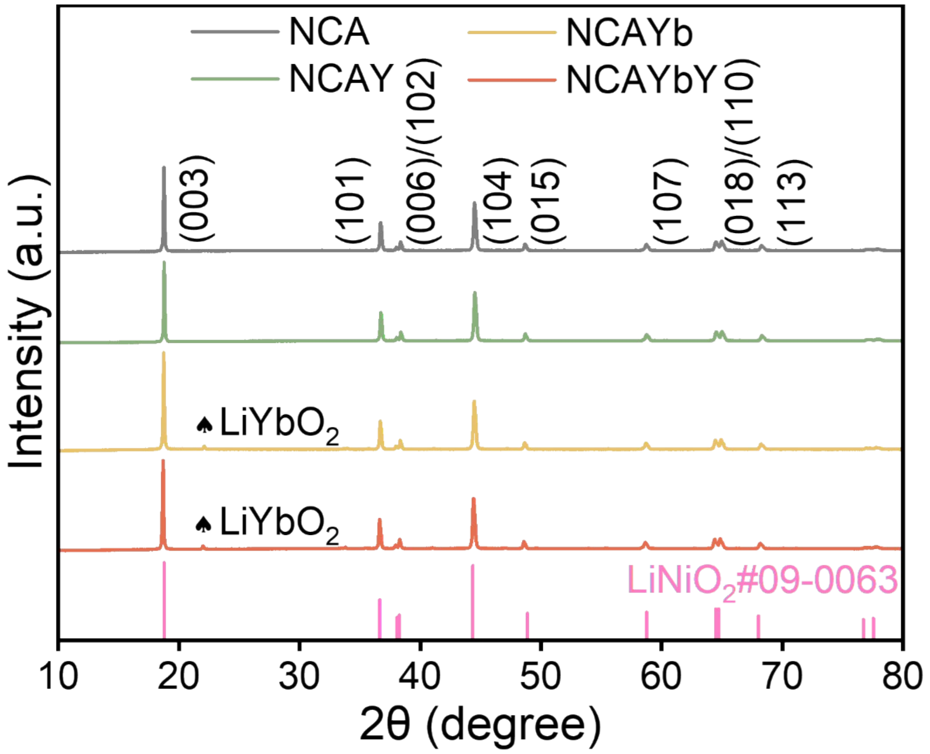

Figure S1. XRD patterns of NCA, NCAY, NCAYb, and NCAYbY.

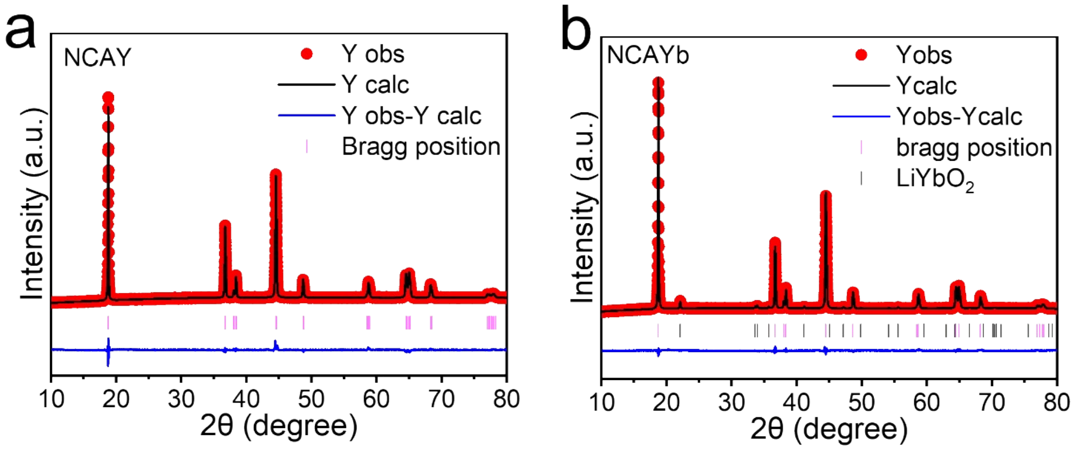

Figure S2. Rietveld refinements of the XRD patterns of (a) NCAY and (b) NCAYb.

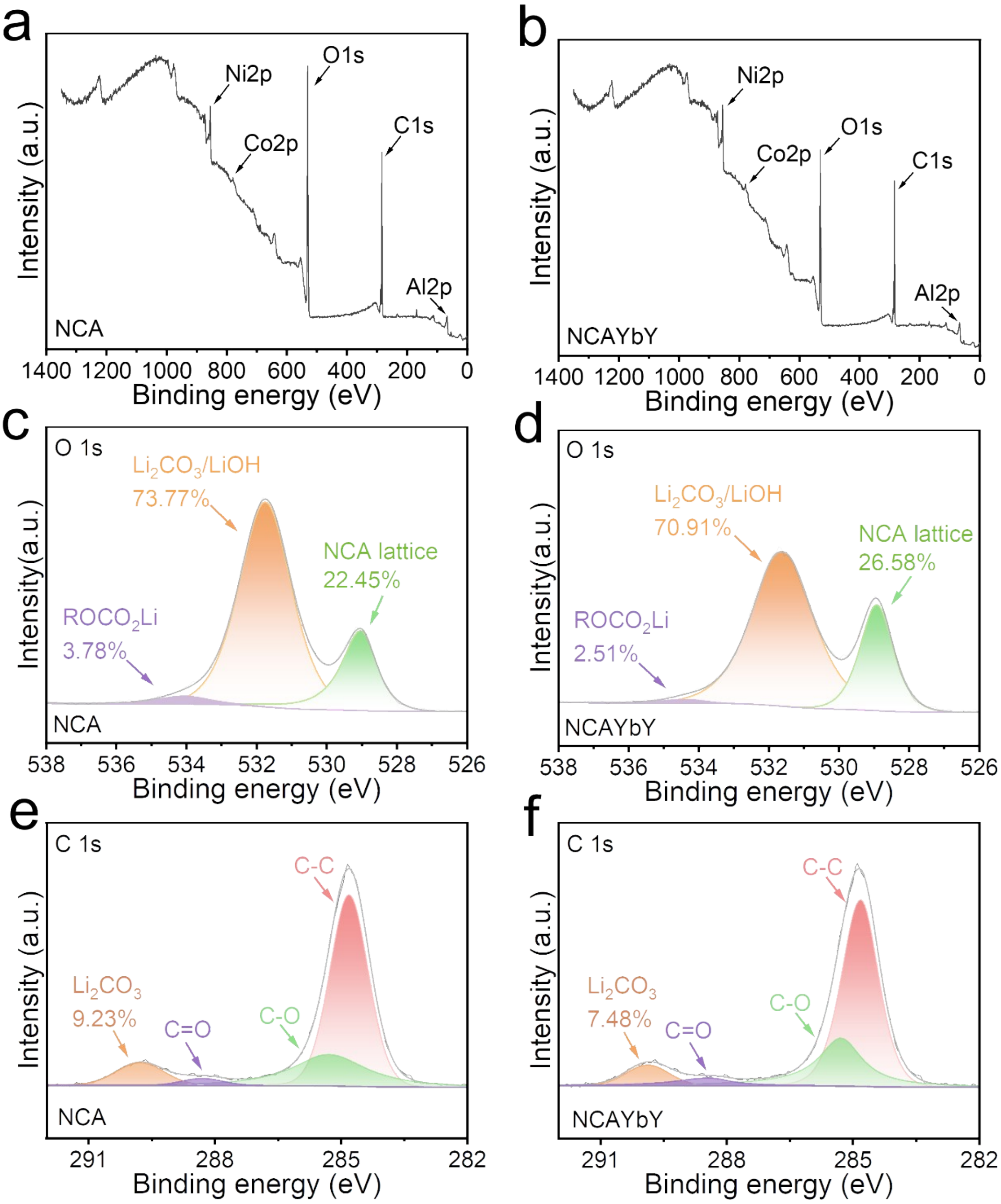

Figure S3. XPS spectra and fitting results of the NCA and NCAYbY cathode materials: (a, b) full spectra, (c, d) O 1s spectra, (e, f) C 1s spectra.

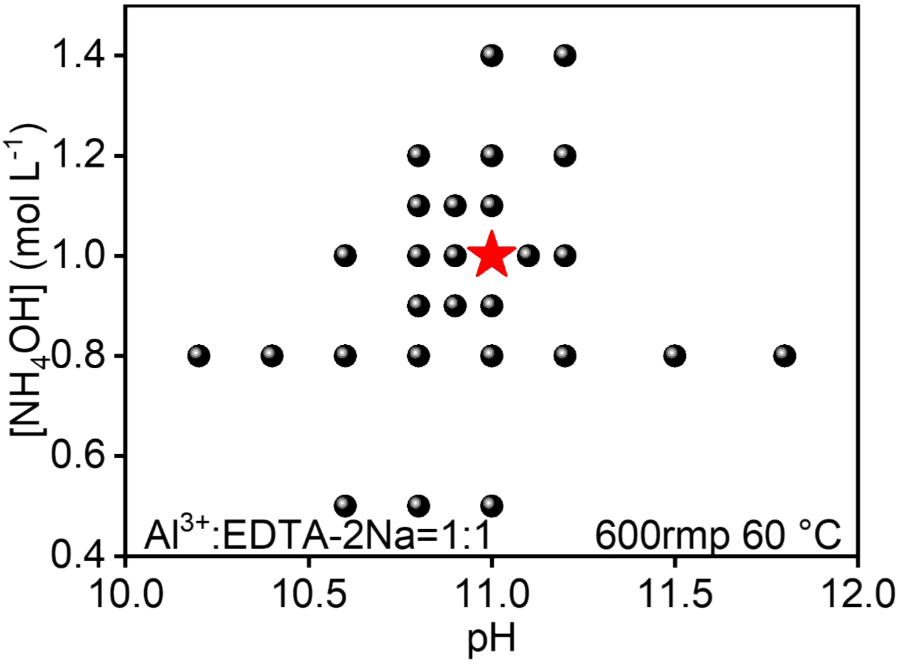

Figure S4. Key process parameters for precursors synthesized under different reaction conditions.

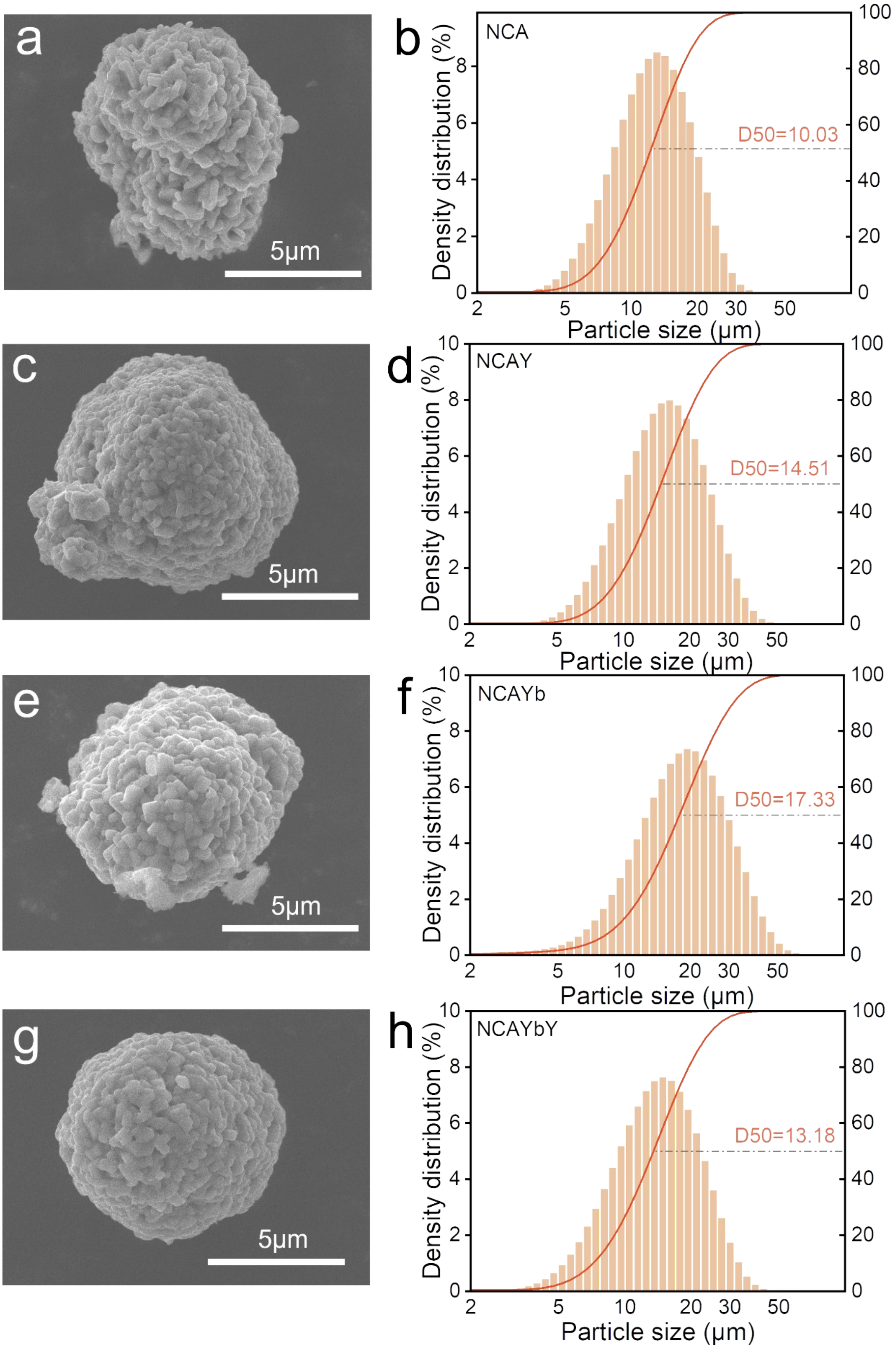

Figure S5. SEM images and particle size distributions of (a,b) NCA, (c,d) NCAY, (e,f) NCAYb, and (g,h) NCAYbY particles.

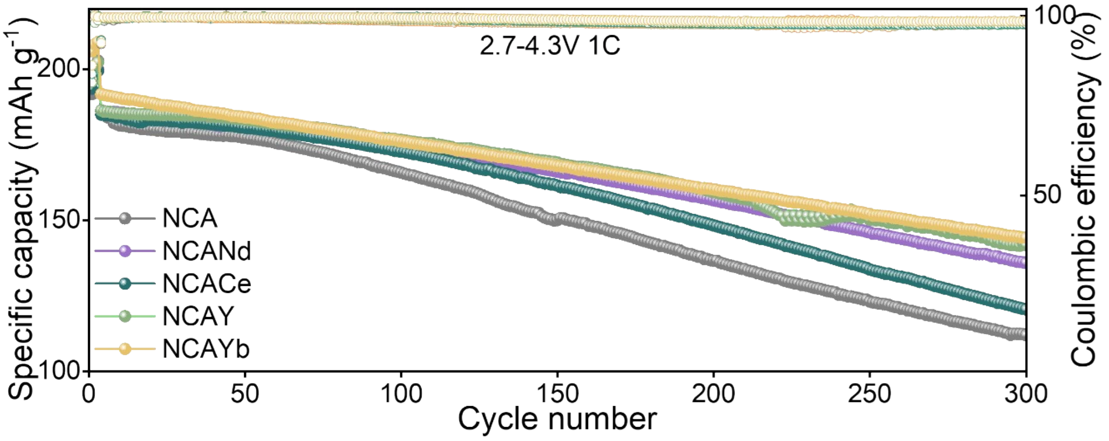

Figure S6 Cycling performance of single-element doped samples at 1 C.

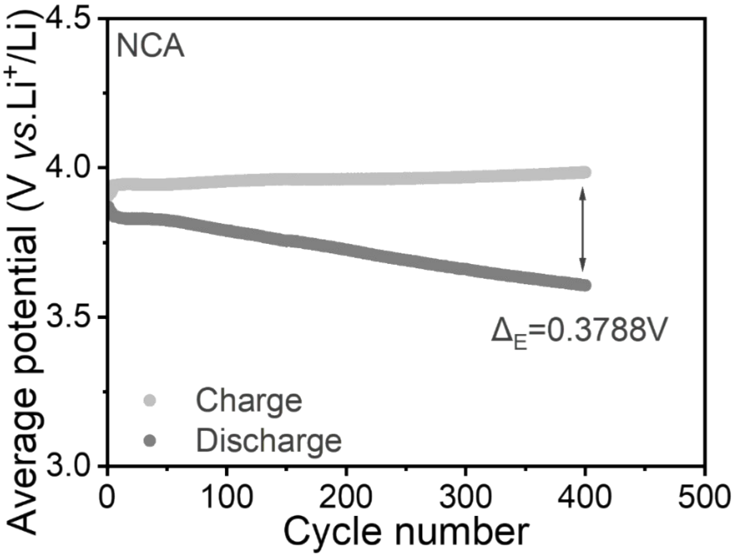

Figure S7. Average charge and discharge potentials of NCA.

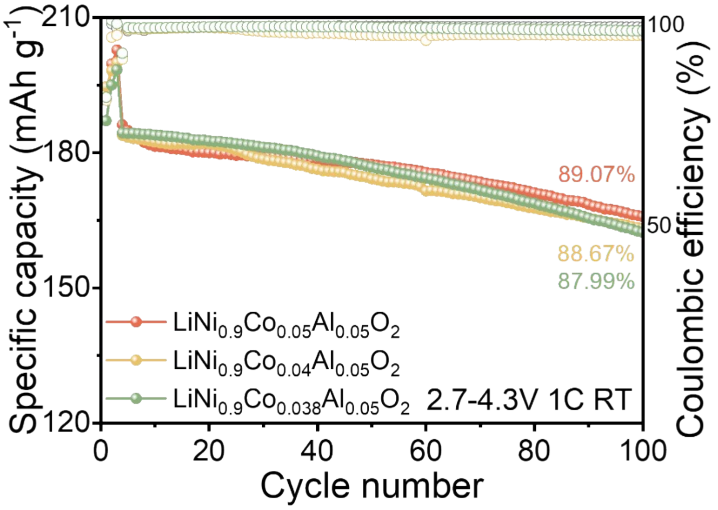

Figure S8 Cycle performance of undoped NCA cathodes with different Co content levels at 1C.

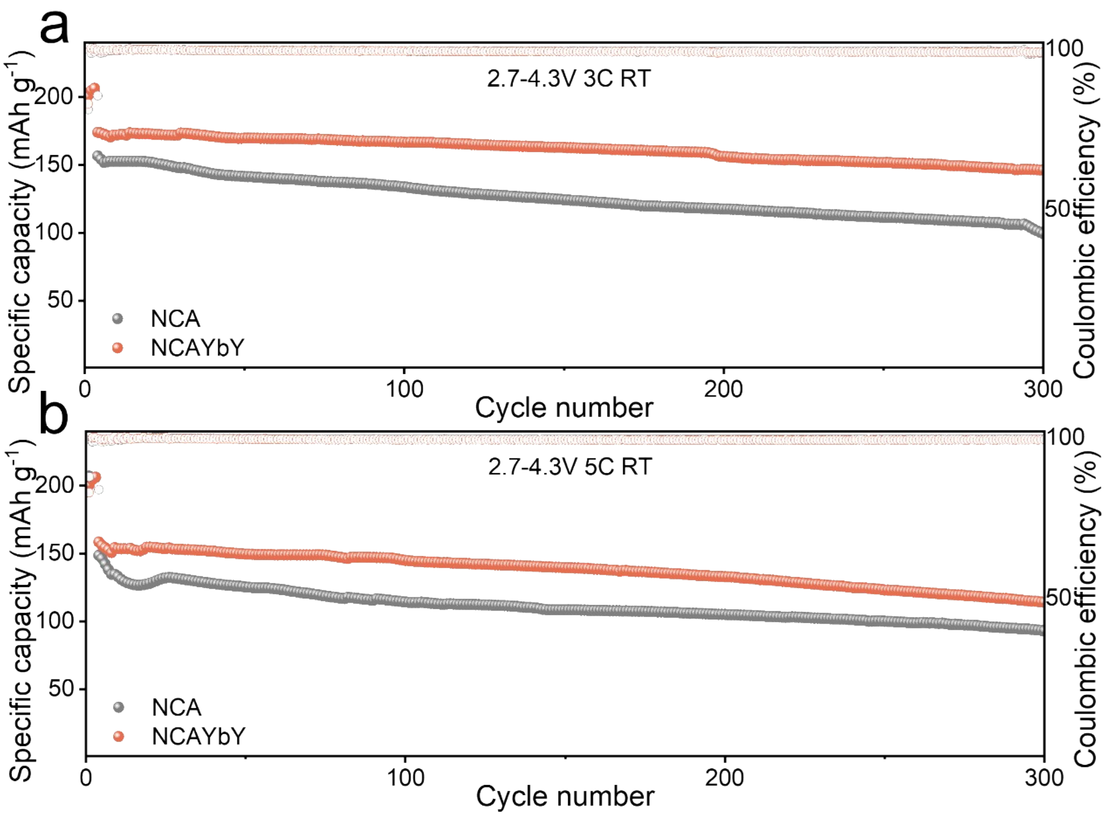

Figure S9. Cycling performances of NCA and NCAYbY at (a) 3 C and (b) 5 C.

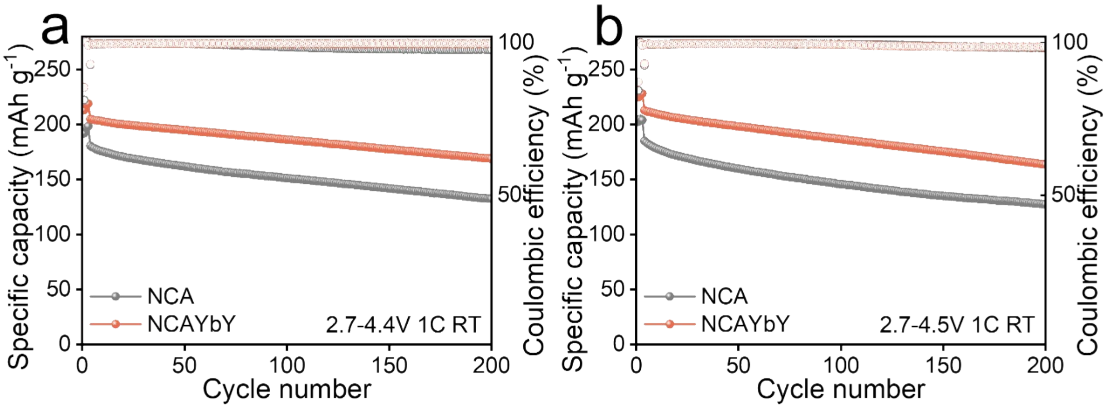

Figure S10. Cycling performance of NCA and NCAYbY tested between (a) 2.7–4.4 V and (b) 2.7–4.5 V.

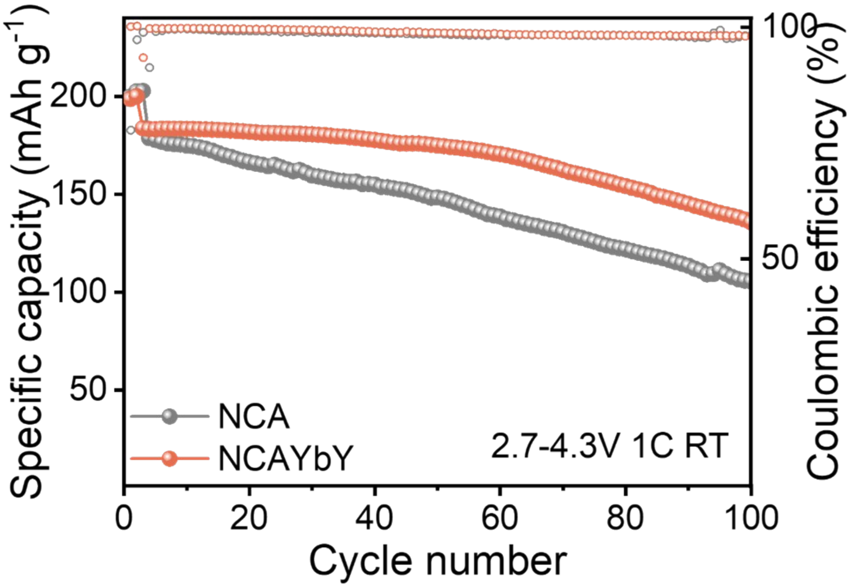

Figure S11. Cycling performance of NCA and NCAYbY under a high mass loading (~7 mg cm^{-2}).

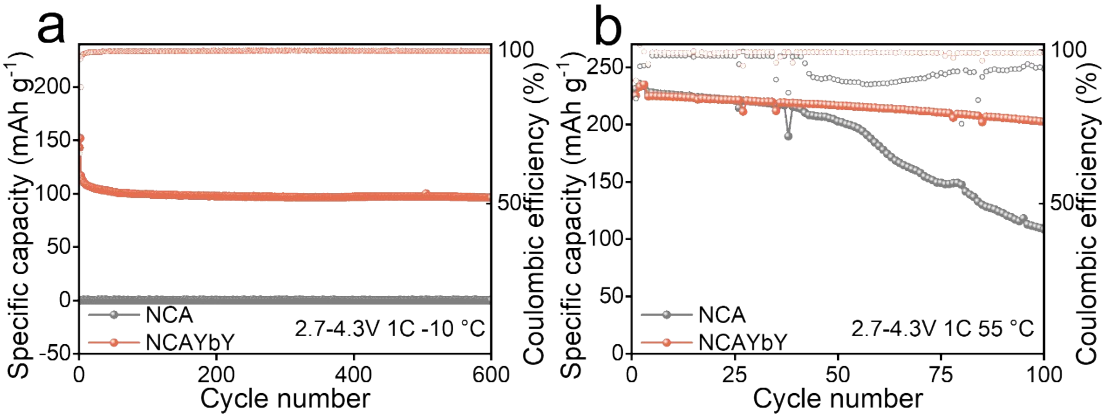

Figure S12. Cycling performance of NCA and NCAYbY at (a) -10°C and (b) 55°C.

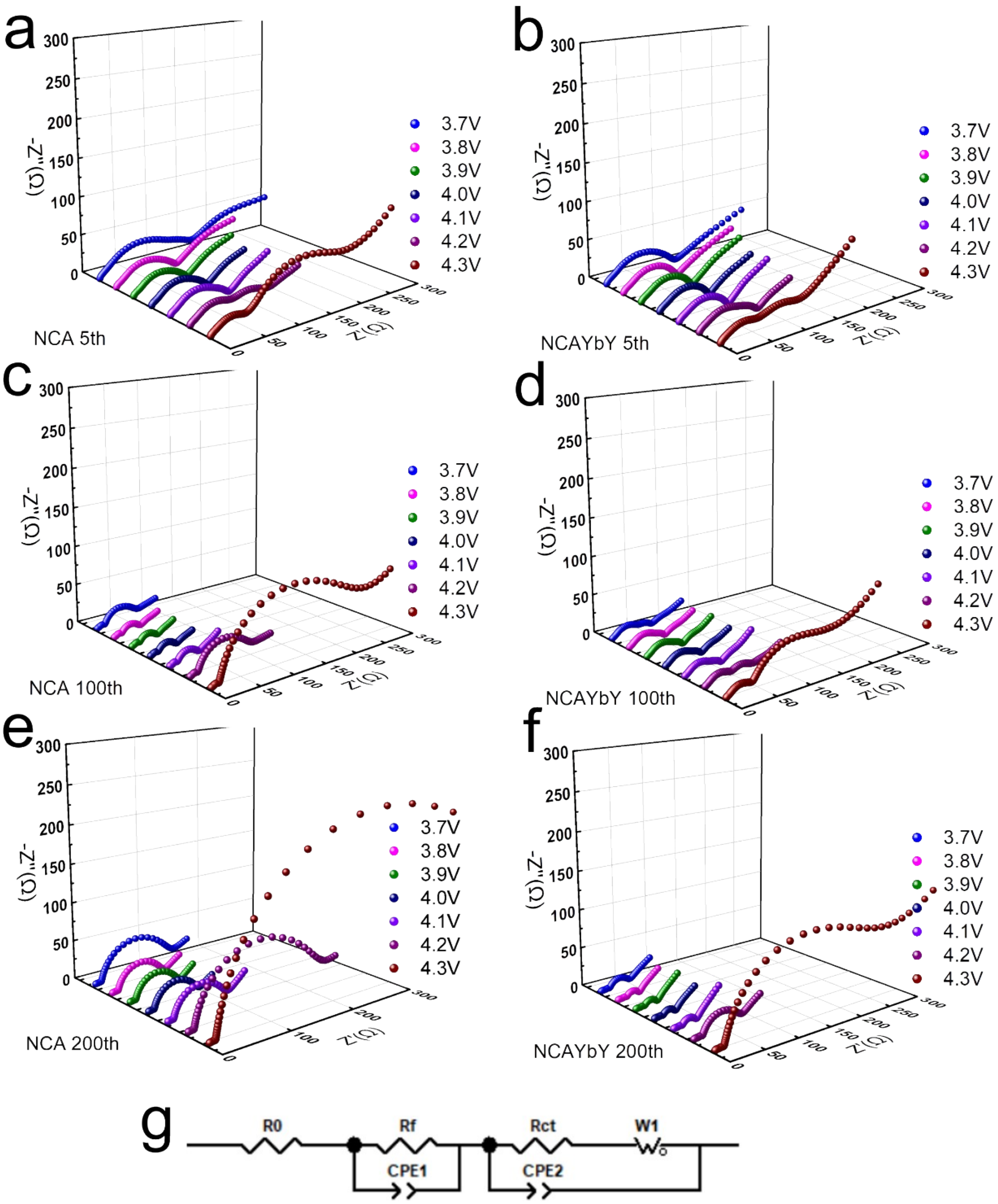

Figure S13. In situ EIS Spectra of (a) NCA and (b) NCAYbY at the 5th cycle; (c) NCA and (d) NCAYbY at the 100th cycle; (e) NCA and (f) NCAYbY at the 200th cycle; (g) equivalent circuit model used for fitting the EIS plots.

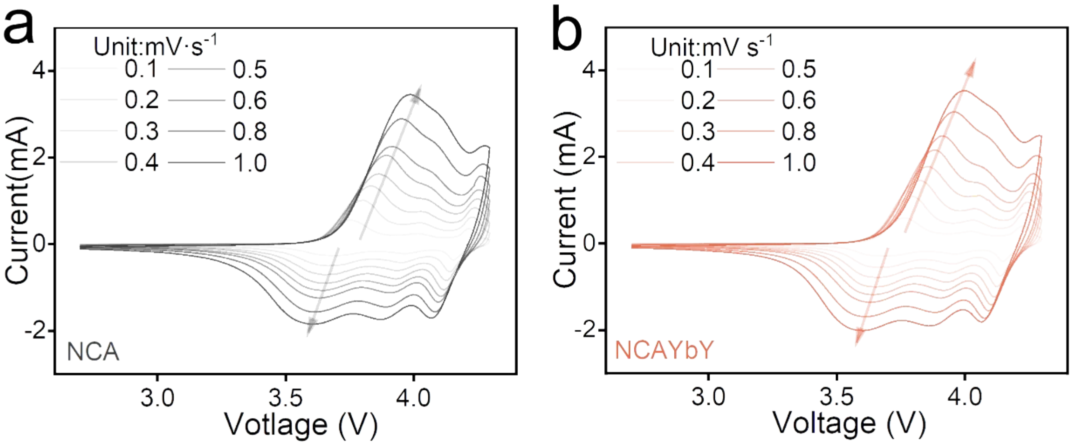

Figure S14. CV curves of (a) NCA and (b) NCAYbY at various scan rates.

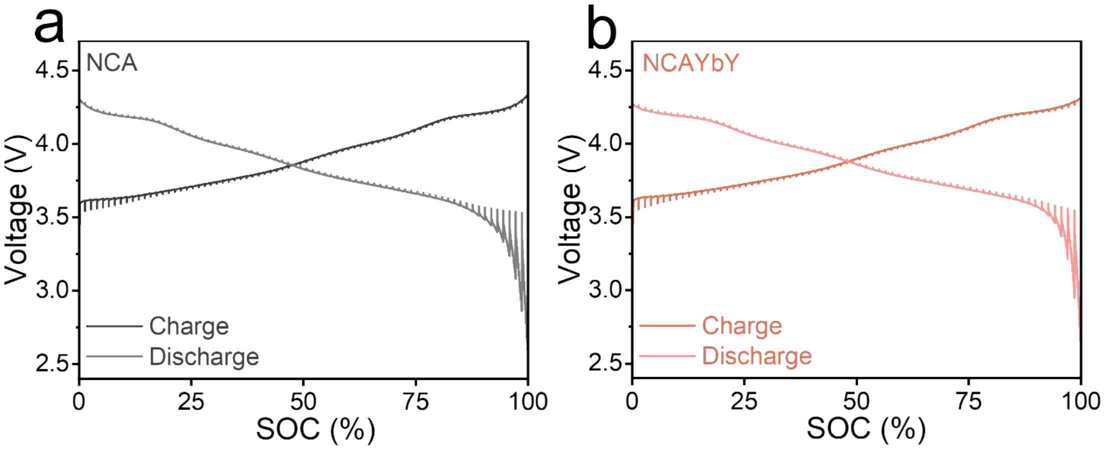

Figure S15. GITT curves of (a) NCA and (b) NCAYbY.

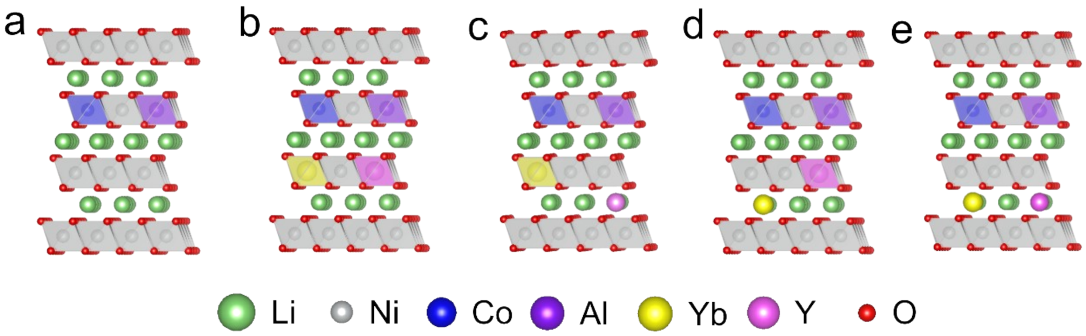

Figure S16. Schematic diagrams of crystal structures for DFT calculations: (a)NCA, (b)Yb@TM / Y@TM, (c)Yb@TM /Y@Li, (d)Yb@Li /Y@TM, and (e)Yb@Li /Y@Li.

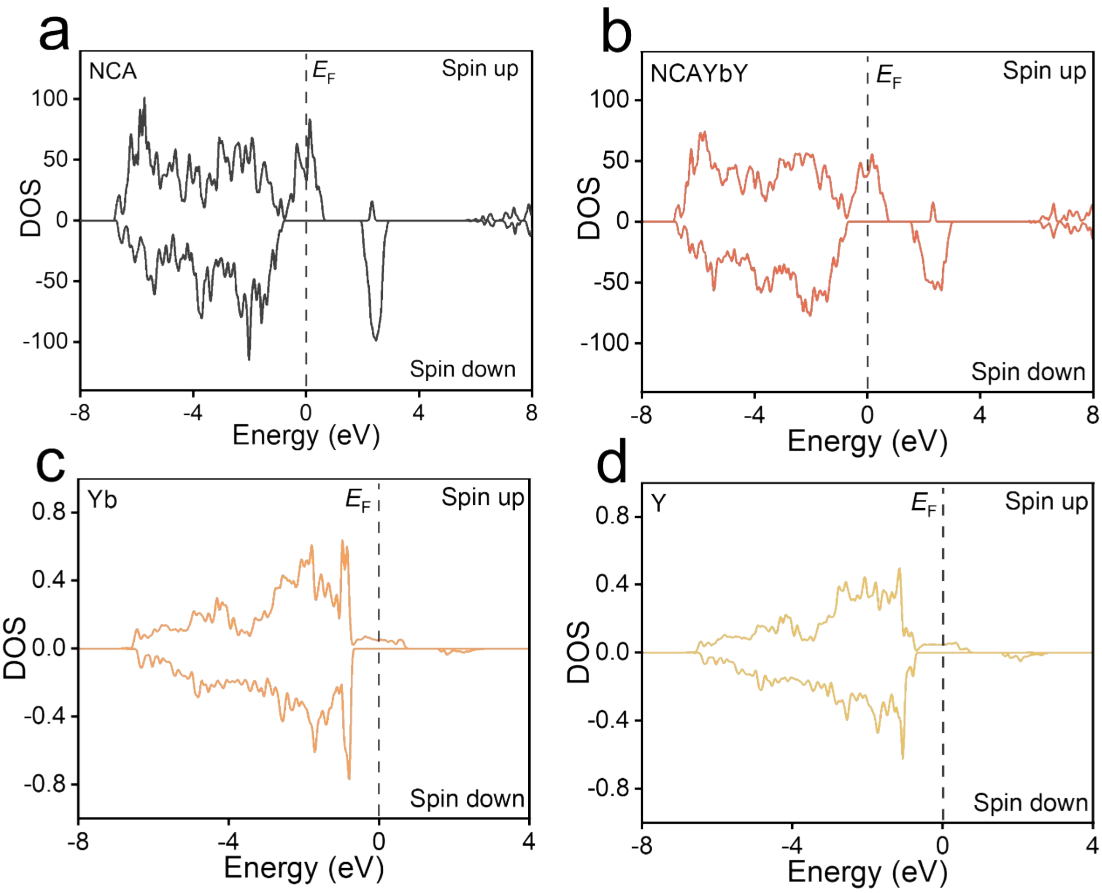

Figure S17. Density of states (DOS) of (a) NCA and (b) NCAYbY; partial density of states (pDOS) of (c) Yb and (d) Y in the cathode structural model.

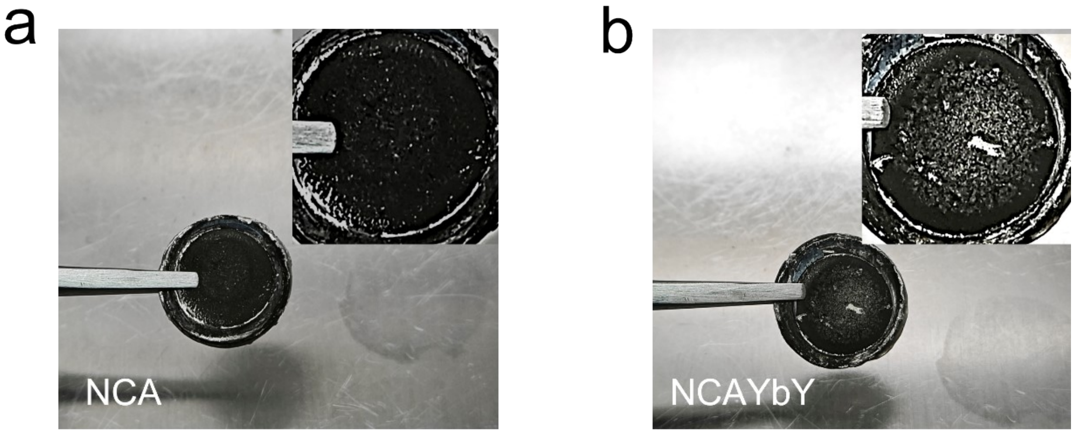

Figure S18. Photographs of the lithium anodes after 100 cycles with (a) NCA and (b) NCAYbY cathodes.

Table S1. Structural parameters obtained from Rietveld refinement of NCA, NCAY, NCAYb, and NCAYbY.

Samples	**NCA**	**NCAY**	**NCAYb**	**NCAYbY**
a **(Å)**	2.86924	2.86764	2.87128	2.87037
c **(Å)**	14.19873	14.19030	14.20674	14.20217
c/a	4.94860	4.94842	4.94787	4.94785
V ($Å^3$)	101.23087	101.05818	101.43027	101.33524
$I_{(003)}/I_{(104)}$	1.65	1.57	1.89	1.68
Ni^{2+}/Li^{+} (%)	6.0	3.4	3.6	2.4
TM-slab (Å)	2.21994	2.20356	2.16107	2.19162
Li-slab (Å)	2.51298	2.52654	2.57442	2.54243
$W_{R\bar{3}m}$	–	–	98.86%	98.84%
$W_{141/amd}$	–	–	1.14%	1.16%
R_p (%)	1.78	2.18	1.69	1.52
R_{wp} (%)	2.42	3.21	2.19	2.16

Table S2. Chemical compositions of NCA and NCAYbY.

Sample	**Chemical composition (at. %)**				
	Ni	Co	Al	Yb	Y
NCA	0.89663	0.05093	0.05244	0	0
NCAYbY	0.89594	0.03865	0.05362	0.00999	0.00180

Table S3. Comparison of specific discharge capacity and cycle stability of Ni-rich NCA cathode materials reported in lithium-ion battery literature.

Cathode composition	Voltage range (V)	Temp. (°C)	1st discharge capacity (mAh g^{-1}/C)	Cycling stability	Ref.
$LiNi_{0.9}Co_{0.038}Al_{0.05}Yb_{0.01}Y_{0.002}O_2$	**2.7-4.3**	**RT**	**192.35 (1 C)**	**96.11% (1 C,100 cycles) 90.80% (1 C,200 cycles)**	**This work**
$LiNi_{0.915}Mn_{0.0475}Al_{0.0106}Mg_{0.0106}Nb_{0.0068}Mo_{0.0095}O_2$	2.8-4.3	RT	~180 (1 C)	85.75% (1 C,100 cycles)	10
LBO coating $LiNi_{0.7}Co_{0.1}Mn_{0.198}Sr_{0.01}Ti_{0.01}O_2$	2.7-4.3	RT	~160 (1 C)	95.2% (1 C,100 cycles)	11
Hf-doped $LiNi_{0.90}Co_{0.05}Mn_{0.05}O_2$	3.0-4.3	30 °C	~184 (1 C)	95.0% (1 C,100 cycles)	12
Mo/F co-doped $LiNi_{0.92}Co_{0.04}Mn_{0.04}O_2$	3.0-4.35	RT	~192 (1 C)	93% (1 C,100 cycles)	13
Sb_2Se_3 -coated and Sb^{5+} doped $LiNi_{0.90}Co_{0.05}Mn_{0.05}O_2$	3.0-4.3	30 °C	~182 (1 C)	96.6% (1 C,100 cycles)	14
$Li_{1.3}W_{0.15}Ti_{1.7}(PO_4)_3$ (LWTP) coating $LiNi_{0.9}Mn_{0.1}O_2$	3.0-4.3	RT	~186 (1 C)	80.4% (1 C,100 cycles)	15
Ta-doped $LiNi_{0.90}Co_{0.04}Mn_{0.03}Al_{0.03}O_2$	2.8-4.3	RT	~165 (1 C)	92% (1 C,200 cycles)	16
La/Mg co-doped $LiNi_{0.83}Co_{0.11}Mn_{0.06}O_2$	3.0-4.3	RT	~189.9 (1 C)	95% (1 C,100 cycles)	17
Rock salt passivation layer coating $LiNi_{0.6}Co_{0.2}Mn_{0.2}O_2$	3.0-4.3	RT	~172 (1 C)	87.2% (1 C,100 cycles)	18
Ba/Al co-doped $LiNi_{0.85}Co_{0.05}Mn_{0.10}O_2$	2.7-4.3	RT	~181 (1 C)	92.1% (1 C,200 cycles)	19
Na/W co-doped $LiNi_{0.83}Co_{0.12}Mn_{0.5}O_2$	3.0-4.3	RT	~183 (1 C)	85% (1 C,200 cycles)	20
Ti/Mg co-doped $LiNi_{0.89}Co_{0.11}O_2$	2.8-4.3	RT	~189.9 (1 C)	86.5% (1 C,200 cycles)	21
Li_3PO_4 coating and Zr-doped $LiNi_{0.9}Co_{0.1}O_2$	2.8-4.3	RT	~181 (1 C)	80.4% (1 C,200 cycles)	22
$La_2Li_{0.5}Al_{0.5}O_4$ coating and Al^{3+} doped $LiNi_{0.8}Co_{0.1}Mn_{0.1}O_2$	2.8-4.3	RT	~180 (1 C)	90.9% (1 C,200 cycles)	23

Table S4. Charge transfer resistance (R_{ct}) and CEI resistance (R_{CEI}) values for NCA and NCAYbY after different cycles, derived from in situ EIS analysis.

Materials	**Cycle**	**R (Ω)**	**Voltage (V)**						
			4.3	4.2	4.1	4.0	3.9	3.8	3.7
NCA	5th	R_{ct}	196.48	95.71	68.44	72.23	57.83	102.03	129.64
		R_{CEI}	42.44	51.78	57.87	58.95	60.46	65.02	97.32
	100th	R_{ct}	211.41	117.43	73.43	78.76	79.40	104.57	143.73
		R_{CEI}	38.45	33.89	36.22	37.84	38.79	40.03	38.75
	200th	R_{ct}	550.34	195.32	79.98	85.17	88.65	112.97	155.79
		R_{CEI}	18.43	17.11	17.45	17.68	16.22	17.82	18.99
NCAYbY	5th	R_{ct}	101.63	54.12	42.10	35.34	43.32	34.76	36.77
		R_{CEI}	35.85	41.54	55.74	56.45	58.31	64.01	88.12
	100th	R_{ct}	152.23	56.89	46.43	42.78	45.23	44.57	49.94
		R_{CEI}	28.44	29.45	32.03	32.44	34.02	35.14	36.87
	200th	R_{ct}	238.11	74.34	48.78	45.56	46.66	47.68	58.67
		R_{CEI}	12.88	11.67	12.56	12.73	12.81	12.83	13.76

Table S5. XPS depth-dependent compositional evolution of C 1s core levels in cycled NCA.

Etching time (s)	OCO_2 (%)	C=O(%)	C-O (%)	C-C (%)
0	9.68	12.22	18.16	59.94
50	5.97	14.55	6.59	72.90
100	7.18	12.50	13.26	67.07
500	3.75	13.49	12.83	69.93

Table S6. XPS depth-dependent compositional evolution of C 1s core levels in cycled NCAYbY.

Etching time (s)	OCO_2 (%)	C=O (%)	C-O (%)	C-C (%)
0	11.15	12.35	20.48	56.02
50	7.60	10.23	9.29	72.88
100	11.25	4.40	11.37	72.98
500	6.48	6.02	11.00	76.50

Table S7. XPS depth-dependent compositional evolution of O 1s core levels in cycled NCA.

Etching time (s)	O-C=O (%)	C=O (%)	TM-O (%)
0	35.59	60.14	4.27
50	30.40	63.78	5.81
100	25.59	67.88	6.53
500	19.05	73.20	7.76

Table S8. XPS depth-dependent compositional evolution of O 1s core levels in cycled NCAYbY.

Etching time (s)	O-C=O (%)	C=O (%)	TM-O (%)
0	46.15	52.31	1.54
50	25.13	69.73	5.14
100	22.58	70.62	6.80
500	18.70	69.24	12.06

Table S9. XPS depth-dependent compositional evolution of F 1s core levels of NCA.

Etching time (s)	C-F (%)	$Li_xPF_yO_z$ (%)	Li-F (%)
0	3.33	61.93	34.74
50	4.65	16.65	78.71
100	3.36	10.51	86.13
500	4.59	8.62	86.79

Table S10. XPS depth-dependent compositional evolution of F 1s core levels of NCAYbY.

Etching time (s)	C-F (%)	$Li_xPF_yO_z$ (%)	Li-F (%)
0	8.39	47.77	43.84
50	5.42	9.10	85.48
100	4.42	6.89	88.69
500	3.77	2.38	93.85

References

1 G. Kresse and J. Furthmüller, *Phys. Rev. B*, 1996, **54**, 11169–11186.

2 G. Kresse and D. Joubert, *Phys. Rev. B*, 1999, **59**, 1758–1775.

3 P. E. Blöchl, *Phys. Rev. B*, 1994, **50**, 17953–17979.

4 J. P. Perdew, J. A. Chevary, S. H. Vosko, K. A. Jackson, M. R. Pederson, D. J. Singh and C. Fiolhais, *Phys. Rev. B*, 1992, **46**, 6671–6687.

5 J. P. Perdew, K. Burke and M. Ernzerhof, *Phys. Rev. Lett.*, 1996, **77**, 3865–3868.

6 S. L. Dudarev, G. A. Botton, S. Y. Savrasov, C. J. Humphreys and A. P. Sutton, *Phys. Rev. B*, 1998, **57**, 1505–1509.

7 S. Laubach, S. Laubach, P. C. Schmidt, D. Ensling, S. Schmid, W. Jaegermann, A. Thißen, K. Nikolowski and H. Ehrenberg, *Phys. Chem. Chem. Phys.*, 2009, **11**, 3278–3289.

8 H. Denawi, P. Karamanis and M. Rérat, *J. Mater. Sci.*, 2021, **56**, 8014–8023.

9 J. Shuai, H. Geng, Y. Lan, Z. Zhu, C. Wang, Z. Liu, J. Bao, C.-W. Chu, J. Sui and Z. Ren, *Proc. Natl. Acad. Sci. U. S. A.*, 2016, **113**, E4125-4132.

10 J. Zhou, J. Hu, X. Zhou, Z. Shang, Y. Yang and S. Xu, *Energy Environ. Sci.*, 2024, **18**, 347.

11 L. Qin, H. Yu, X. Jiang, L. Chen, Q. Cheng and H. Jiang, *Sci. China Mater.*, 2024, **67**, 650–657.

12 Y. Zou, Y. Tang, S. Zhou, H. Zhang, J. Chen, Y. Yan, H. Cao, J. Xu, W. Yin, H.-G. Liao, Y. Qiao, J. Bao and S.-G. Sun, *Energy Storage Mater.*, 2024, **69**, 103400.

13 X. He, J. Shen, B. Zhang, Z. Xiao, L. Ye, Q. Mao, Q. Zhong and X. Ou, *Adv. Funct. Mater.*, 2024, **34**, 2401300.

14 Y. Zou, Y. Tang, Q. Zheng, H. Zhang, Y. Yan, J. Xue, S. Zhou, J. Xu, W. Yin, H.-G. Liao, Y. Qiao, J. Bao and S.-G. Sun, *Adv. Funct. Mater.*, 2024, **34**, 2406068.

15 H. Feng, Y. Xu, Y. Hou, F. Zhuge and Q. Tan, *J. Mater. Chem. A*, 2025, **13**, 24772–24784.

16 J. Jeyakumar, M. Seenivasan, T. H. Mengesha, L.-Y. Kuo, S. Sampathkumar, Q.-T. Pham, J. Ling, C.-S. Chern, B. J. Hwang, C.-C. Yang and Y.-S. Wu, *Compos. Part B Eng.*, 2026, **311**, 113287.

17 K. Li, W. Chen, M. Duan, Z. Liu, D. Muhtar, X. Yang, K. Ning, F. Xie and X. Lu, *Small*, 2025, **21**, 2502152.

18 Y. Shen, Z. Tang, D. Yin, A. Chen, L. Wang, L. Wang, X. Zhang and Y. Cheng, *Nano Res.*, 2024, **18**, 94907599.

19 H. Zhang, L. Qin, M. Sedlacik, P. Saha, Q. Cheng, H. Yu and H. Jiang, *J. Mater. Chem. A*, 2024, **12**, 3682–3688.

20 J. Shen, H. Li, H. Qi, Z. Lin, Z. Li, C. Zheng, W. Du, H. Chen and S. Zhang, *J. Energy Chem.*, 2024, **88**, 428–436.

21 Y. Xie, F. Guo and Y. Zhang, *J. Alloys Compd.*, 2024, **981**, 173592.

22 L. Li, Q. Ran, S. Hao, Y. Ji, W. Cheng and X. Liu, *J. Colloid Interface Sci.*, 2022, **615**, 554–562.

23 Y. Liu, T. Zeng, G. Li, T. Wan, M. Li, X. Zhang, M. Li, M. Su, A. Dou, W. Zeng, Y. Zhou, R. Guo and D. Chu, *Energy Storage Mater.*, 2022, **52**, 534–546.